Complexes of Platinum Group Metals with a Conformationally Locked Scorpionate in a Metal–Organic Framework: An Unusually Close Apical Interaction of Palladium(II)

Complexes of Platinum Group Metals with a Conformationally Locked Scorpionate in a Metal-Organic Framework: An Unusually Close Apical Interaction of Pd(II)

*Michael T. Payne[1], Constanze N. Neumann[1†], Eli Stavitski[2], and Mircea Dincă[1]**

[1]Department of Chemistry, Massachusetts Institute of Technology, 77 Massachusetts Avenue, Cambridge, Massachusetts 02139, United States

[2]National Synchrotron Light Source II, Brookhaven National Laboratory, Upton, New York 11973, United States

KEYWORDS

ABSTRACT. We report synthetic strategies for installing platinum group metals (PGMs: Pd, Rh, Ir, and Pt) on a scorpionate-derived linker (TpmC*) within a metal-organic framework (MOF), both by room-temperature post-synthetic metallation and by direct solvothermal synthesis, with a wide range of metal loadings relevant for fundamental studies and catalysis. In-depth studies for the palladium adduct, Pd(II) @Zr-TpmC*, by density functional theory-assisted extended X-ray absorption fine structure spectroscopy (DFT-assisted EXAFS) reveals that the rigid MOF lattice enforces a close Pd(II)-N_{apical} interaction between the bidentate Pd complex and the third

uncoordinated pyrazole arm of the TpmC* ligand (Pd-N_{apical} = 2.501 ± 0.067 Å), an interaction which is wholly avoided in molecular Pd scorpionates.

INTRODUCTION

The scorpionate ligands trispyrazolylborate (Tp) and trispyrazolylmethane (Tpm), introduced by Trofimenko in the late 1960s,[1] can tightly chelate a metal by facial κ^3 coordination while retaining open cis-oriented coordination sites. The resulting stable metal complexes are capable of concerted oxidative addition and reductive elimination. This has enabled fundamental studies in properties of 2nd and 3rd row transition metals, exemplified by Canty's use of scorpionates to stabilize high oxidation state organometallic complexes of palladium and platinum,[2] as well as novel reactivity, such as the C–H activation chemistry of rhodium, iridium, and ruthenium scorpionates.[3]

The coordination chemistry of scorpionates, however, can be challenging to control in molecular systems: coordination sites required for catalysis are often blocked via intermolecular pathways such as homoleptic ML_2 complex formation and $(ML)_2$ dimerization (Figure 1a). Undesired intermolecular interactions are exacerbated by the rotational lability of the pyrazole rings, which allows the scorpionate to bridge multiple metals while also opening additional ligand degradation pathways via intramolecular C–H activation. These destructive pathways can be blocked by installation of bulky substituents on the pyrazole rings,[4] but such ligands are often difficult to synthesize, and steric encumbrance of the active site limits both metal ligation and overall catalyst activity.

In principle, bimolecular deactivation or decomposition pathways can be eliminated altogether by immobilizing the ligand in a solid matrix, locking the conformation and position of the scorpionate. Metal-organic frameworks (MOFs) are privileged among solid-state materials due to

their modular structure and molecular tunability, offering a capacity for design and optimization ideal for supporting well-defined metal complexes.[5] In the case of first-row transition metals, heterogenization of scorpionate-based catalysts in the MOFs MFU-4*l* and CFA-1 led to long-lived catalysts that replicated the characteristic reactivity of their molecular analogs while eschewing bimolecular deactivation pathways.[6–12] The requisite catalytically active transition metal centers were installed into the secondary building unit (SBU) by cation exchange of structural metals, but the widespread success of this strategy for first-row transition metals has not translated to PGMs. To our knowledge, there is only one reported introduction of a 2nd- or 3rd-row transition metal containing a partially filled d-shell into an SBU.[13]

Alternatively, single-site installation of a reactive metal on the linker of a MOF produces a well-defined heterogeneous catalyst that can be studied and tuned with molecular precision.[14–16] Beyond simply translating homogeneous systems to solid supports, site-isolation in a MOF can confer new catalytic properties by modulating the catalyst microenvironment, restricting ligand flexibility, and stabilizing against biomolecular decomposition;[17] thus, methodologies for producing new MOF-supported metal species offer the means to access new reactivity with existing catalysts. Recently, our group reported a MOF composed of a Tpm-based linker, $\{(TpmC^*)_8[Zr_6O_4(OH)_4(X)_4(H_2O)_4]_3\}$ (Zr-TpmC*, X = HO^- or $HCOO^-$).[18] Attempts at direct solvothermal synthesis of Zr-TpmC* lead to exclusive formation of amorphous materials, which we attributed to the conformational flexibility of the free ligand. However, TpmC* could be templated *in situ* with rigid C_{3v} symmetry, required for the Zr-TpmC* framework, via metallation with CuI during MOF synthesis to produce crystalline CuI@Zr-TpmC*. Subsequent treatment of CuI@Zr-TpmC* with 1 M HCl removed templating equivalents of CuI to yield crystalline free-base Zr-TpmC* (Scheme S2). We hypothesized that free-base Zr-TpmC* would be capable of

supporting PGM scorpionates without the need for SBU cation exchange. Indeed, we found that the free base MOF could be readily metallated with suitable precursors to yield the corresponding Pd, Rh, Ir and Pt scorpionate complexes within a heterogeneous host (Figure 1b,c). PGM@Zr-TpmC* represent the first report of MOF-supported second and third row transition metal scorpionates. Both high PGM loadings, ideal for mechanistic and structural studies, and low metal loadings that minimize mass transfer limitations in catalytic applications could be accessed.

We demonstrate that Ir@Zr-TpmC* and Rh@Zr-TpmC* are readily prepared not only by post-synthetic modification of free-base Zr-TpmC*, but also by direct solvothermal synthesis of the MOF in the presence of $IrCl_3$ and $RhCl_3$, which coordinate to TpmC* and template the ligand with C_{3v} symmetry, thereby avoiding the laborious Cu-templation and demetallation steps (*vide supra*). The two complimentary synthetic pathways provide access to a diverse suite of PGM@Zr-TpmC* systems (Figure 1b), and lay the foundation for the introduction of a wide range of elements into MOF-supported scorpionates. Further investigation by X-ray Absorption Spectroscopy (XAS) and complementary density functional theory (DFT) calculations revealed that the MOF support can impart a unique PGM coordination environment that is distinct from the corresponding molecular complex, as was the case for the geometrically frustrated interaction of the TpmC* metallo-ligand with square planar Pd(II). We observe that the rigid MOF lattice enforces an unusually short Pd(II)–N_{apical} interaction (2.501 Å), which we attribute to the metallo-ligand being conformationally locked in C_{3v} symmetry by the MOF framework. In molecular systems, short interatomic distances between square planar Pd(II) centers and elements capable of acting as axial ligands are reported to lower the oxidation potential of Pd(II), and concomitantly stabilize the +III and +IV oxidation state.[19,20] The short Pd–N_{apical} interaction enforced by the MOF support and limited molecular motion required for the coordination of an axial ligand suggests that Pd(II)@Zr-

TpmC* may display low barrier for the oxidation of Pd, a desirable feature in high-valent palladium catalysis.

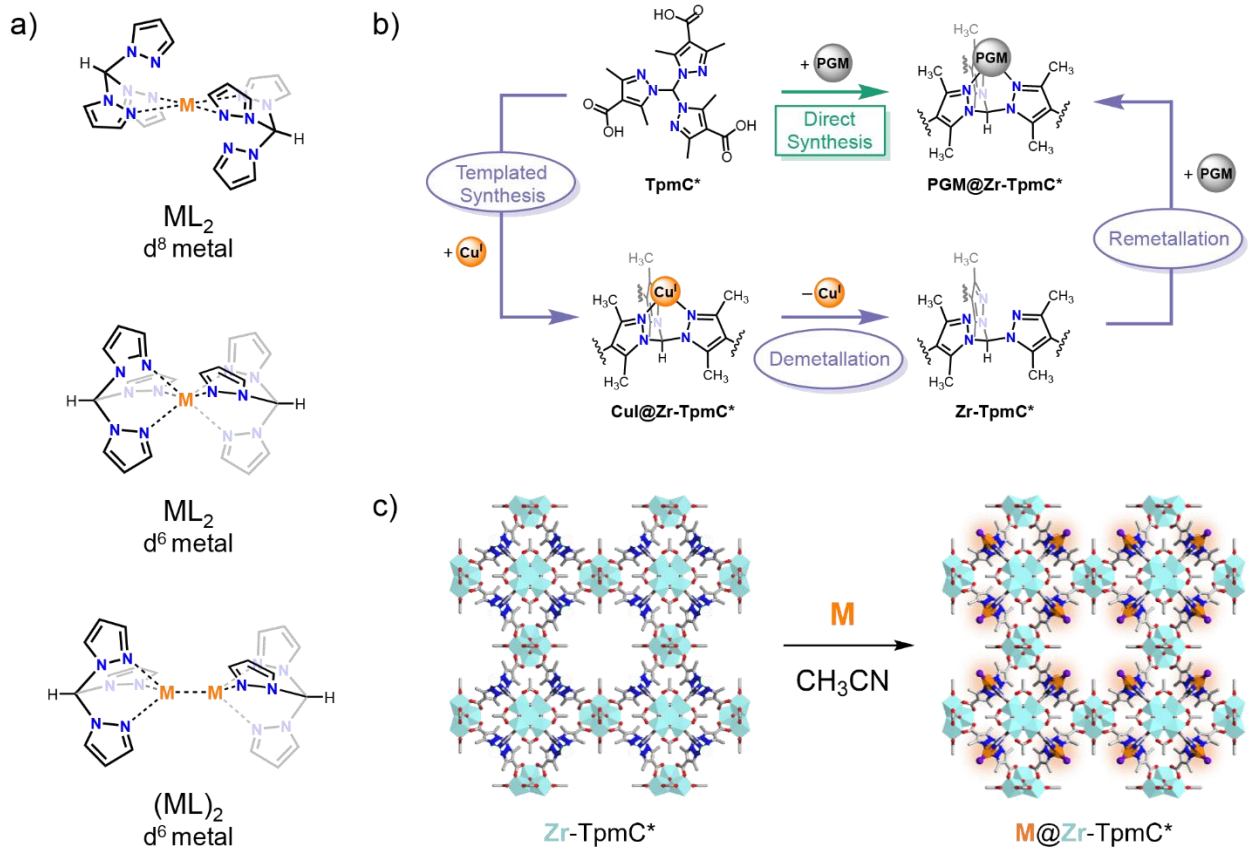

Figure 1. (a) Deactivation modes of molecular metal scorpionates by homoleptic ML_2 formation and $(ML)_2$ dimerization. (b) Synthetic routes for accessing site-isolated PGM scorpionates using the Zr-TpmC* MOF. (c) Generic scheme for remetallation of Zr-TpmC*

RESULTS AND DISCUSSION

Scorpionate Sites in Zr-TpmC* are Quantitatively Metallated by Palladium(II) via Post-Synthetic Modification. We first pursued the synthesis of a Pd(II)@Zr-TpmC* system using $[Pd(CH_3CN)_4](BF_4)_2$ as a Pd(II) source, based on the assumption that the labile acetonitrile ligands

and weakly coordinating anions would facilitate PGM installation. Activated free-base Zr-TpmC* was soaked in an acetonitrile solution of $[Pd(CH_3CN)_4](BF_4)_2$ containing one equivalent of Pd complex per equivalent of open TpmC* binding site over a period of five days. During this time, the yellow-orange color of the solution faded and the MOF sample changed in color from white to yellow, suggesting that the Pd complex had been absorbed into the framework. The product was recovered, washed and dried to yield a yellow microcrystalline powder which we assign as $[Pd(CH_3CN)_2](BF_4)_2$@Zr-TpmC* (**1**). Characterization of **1** by powder X-ray diffraction (PXRD) shows that the crystallinity of Zr-TpmC* is maintained (Figure 2a) with no signature of Pd nanoparticle formation (Figure S9, see Supporting Information).

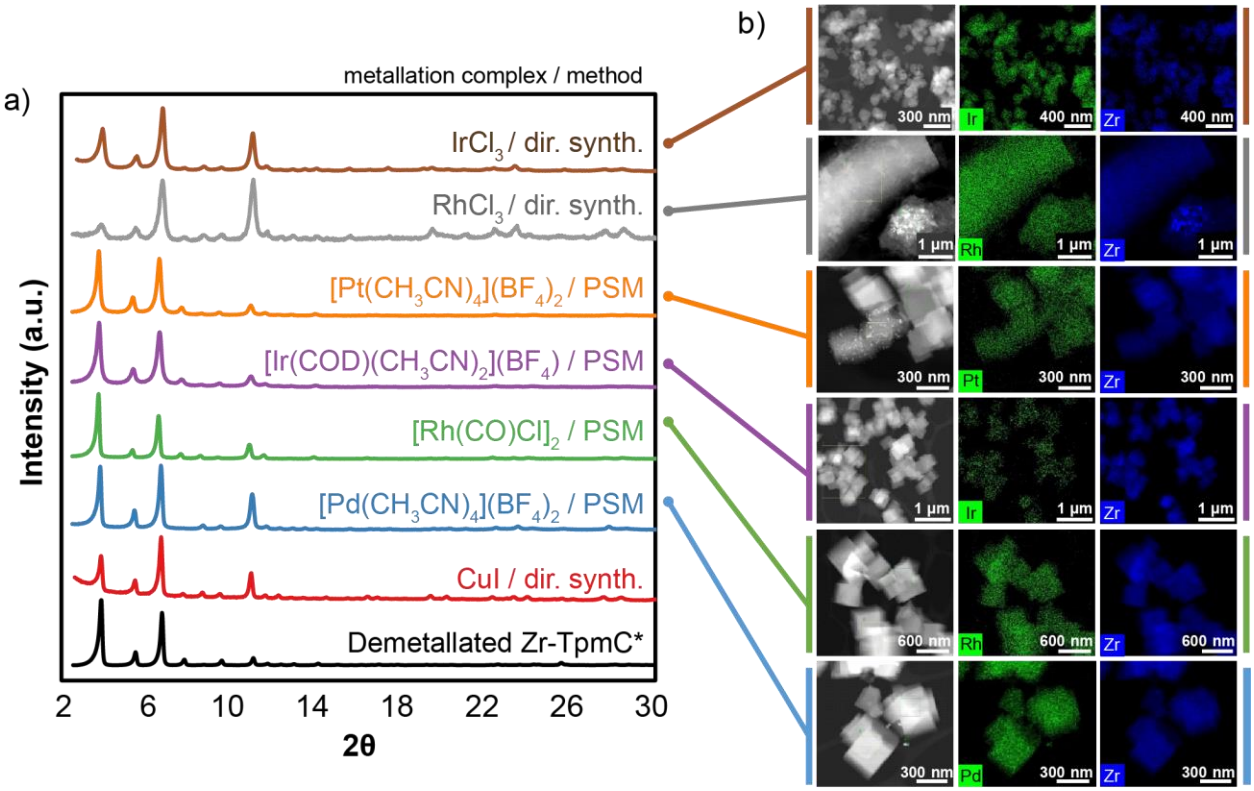

Figure 2. (a) PXRD patterns of PGM@Zr-TpmC*. (b) Transmission Electron Microscopy/Energy-Dispersive X-ray Spectroscopy (TEM/EDS) images of PGM@Zr-TpmC*. PSM = post-synthetic metallation

In our initial report on Zr-TpmC*, we observed that the remetallation of Zr-TpmC* by $[Cu(CH_3CN)_4](BF_4)$ plateaued at four equivalents of Cu per formula unit (50% of available TpmC* sites). In contrast, we achieved nearly complete metallation of Zr-TpmC* using $[Pd(CH_3CN)_4](BF_4)_2$, with up to seven equivalents of Pd installed per formula unit (vs eight available TpmC* sites) as determined by inductively coupled plasma mass spectrometry (ICP-MS). Furthermore, while cation exchange typically requires large excesses of metal for significant incorporation, metallation of Zr-TpmC* by Pd is nearly quantitative, with >80% Pd incorporation at a range of sub-stoichiometric loadings (Figure S11). Such efficient incorporation is essential when preparing catalysts from precious metals such as Pd, given their high costs. Reaction with an excess of $Pd(CH_3CN)_4(BF_4)_2$ does not increase the metal loading to exceed seven equivalents of Pd per formula unit, suggesting that excess Pd does not deposit elsewhere in the framework. Successful metallation of the TpmC* site (and absence of Pd nanoparticles) is corroborated by TEM/EDS imaging of **1**, which showed even incorporation of Pd throughout the Zr-TpmC* crystallites (Figure 2b).

Further experimental characterization of **1** provides evidence that the metallation reagent $Pd(CH_3CN)_4(BF_4)_2$ is ultimately incorporated at the scorpionate sites, losing two acetonitrile ligands to form $[Pd(CH_3CN)_2(TpmC^*)]^{2+}$ units whose charge is balanced by BF_4^- presumably residing in the pores. A PXRD experiment gives direct evidence for uniform introduction of Pd into the scorpionate site, as the 7.8° peak, which corresponds to the (200) reflection, is observed to systematically decrease in intensity with increasing Pd loading (Figure 3a). We attribute this to a phase cancellation phenomenon caused by heavy atoms into the scorpionate sites, which lie directly in-between the (200) planes and thus diffract 180° out-of-phase with the (200) reflection (Figure S13). The acetonitrile ligands bound to Pd in **1** were also detected by infrared spectroscopy

(IR) as weak bands at 2310 cm^{-1} and 2340 cm^{-1} (Figure 3b). These C≡N stretch bands are redshifted by approximately 10 cm^{-1} in comparison with free $[Pd(CH_3CN)_4](BF_4)_2$. We ascribe the redshift to the exchange of two weakly pi-accepting nitrile ligands for the framework pyrazole ligands, which would effectively behave only as sigma donors due to a fixed orientation that gives poor d-π* overlap (see Figure 4b); the backbonding to the remaining nitrile ligands would thus increase and the C–N triple bond would concomitantly weaken. Characterization of **1** digested in D_2SO_4/DMSO-d_6 by ^{19}F nuclear magnetic resonance (NMR) spectroscopy confirmed the presence of BF_4^- as the charge-compensating anion. Although acetonitrile was detected by IR, no acetonitrile was observed in ^1H-NMR of digested **1**. We hypothesize that strong acid and trace water in the digestion conditions may induce hydrolysis of acetonitrile to acetic acid, as acetic acid was observed in the ^1H-NMR spectrum (Figure S7).[21]

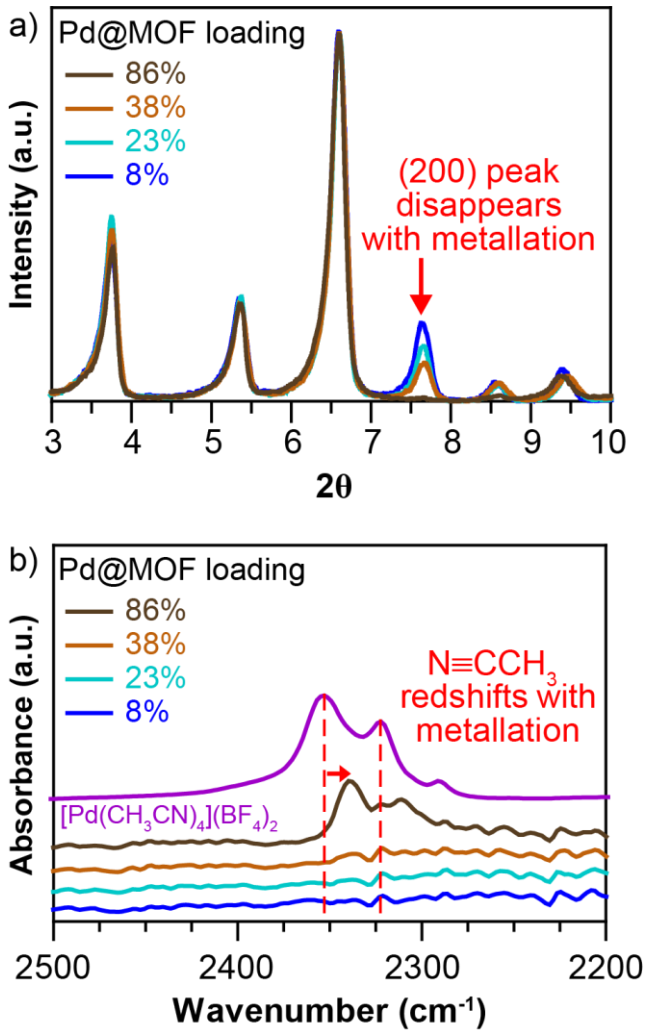

Figure 3. (a) PXRD overlay of Zr-TpmC* samples with varied Pd loading (percentage is vs total accessible TpmC* ligand). (b) IR spectrum overlay of Zr-TpmC* samples with varied Pd loading. Pd loading was determined as Pd content vs. available TpmC* sites by ICP-MS.

Successful incorporation of Pd at the TpmC* scorpionate site in **1** is further evidenced by X-ray photoelectron spectroscopy (XPS) data, which shows an increase of 0.2–0.3 eV in the N 1s binding energy associated with the scorpionate pyrazoles upon metallation and a concomitant decrease of more than 1 eV in the Pd $3d_{5/2}$ binding energy as compared with $[Pd(CH_3CN)_4](BF_4)_2$ (Table S2, see Supporting Information). The observed Pd $3d_{5/2}$ binding energy is consistent with an assignment of the Pd oxidation state in **1** as +II, an assignment which is also supported by solid

state X-ray absorption spectroscopy (XAS) measurements of **1** collected at the Pd K-edge (24350 eV) (Figure S10). Qualitative comparison of the X-ray absorption near-edge structure (XANES) with reference Pd compounds are also consistent with a +II oxidation state and reflect a decrease in the Pd binding energy.

DFT-Assisted EXAFS Characterization of Pd(II)@Zr-TpmC* Reveals Unusually Close Pd-N Apical Interaction. In addition to a confirmation of the metal oxidation state, an XAS study of Pd@Zr-TmpC* was pursued to shed light on the coordination environment of Pd(II), a d^8 metal with a strong electronic preference for square planar geometry, placed in the scorpionate binding site of **2**, which is conformationally locked in C_{3v} symmetry by the MOF lattice (Figure 4a). In molecular Pd(II) scorpionates, the tridentate ligand is coordinated via two of the three pyrazoles in edge-on κ^2 fashion, with the third pyrazole donor rotated 90° to avoid an unfavorable filled-filled interaction with the Pd d_z^2 orbital.[2,22] Upon two-electron oxidation of Pd(II) to the d^6 Pd(IV), the electronic preference shifts to favor octahedral geometry, allowing formation of stable κ^3 scorpionate complexes. Since rotation of the pyrazoles in Zr-TpmC* is inhibited by carboxylate linkages to the SBU, we hypothesized that this rigidity would enforce an unusually close apical interaction between a κ^2 Pd(II) scorpionate and the third pyrazole arm of the ligand. Such an interaction could promote oxidation to a Pd(IV) complex by preconfiguring the Pd for an octahedral geometry.

To directly probe the local coordination environment of Pd in **1**, we employed DFT-assisted extended X-ray absorption fine structure (EXAFS) analysis, an established technique for understanding the local structure of metal atoms in MOFs as well as zeolites, organometallic complexes, and inorganic salts.[23] The initial cluster model used for EXAFS fitting was based on crystallographic data of CuI@Zr-TpmC*,[18] $Pd(Tpm)_2(BF_4)_2$, and $Pd(CH_3CN)_4(BF_4)_2$,[24] and the

model was structurally optimized using DFT (Figure 4a,b). During the geometry optimization, the position of the carboxylic acids was kept fixed to account for the rigidity of the solid structure; analogous protocols have been employed for structure optimization of SBUs in several MOFs.[25–27] Optimized structures which did not include this restraint gave one imaginary frequency involving rotation of the apical pyrazole away from Pd, consistent with the previously mentioned behavior of molecular Pd(II)-scorpionate systems (Figure S39).

The signal/noise ratio of the collected EXAFS data allowed us to fit single scattering (SS) paths from both the first- and second-coordination shells in the R-space interval ΔR = (1.0–3.1) Å. The first coordination shell consists of two acetonitrile N atoms and two pyrazole N atoms in square planar geometry, which were modeled as an averaged 4-atom shell of SS paths (N_1) with a single ΔR and Debye-Waller (σ^2) parameter. The second coordination shell consists of the apical imine N atom of the third pyrazole arm (N_{apical}) and the amine N atoms of the two coordinated pyrazoles (N_2). The obtained fit reproduces our experimental data well (Figure 4c-f), giving Pd–N_1 and Pd–N_2 bond distances which are in good agreement with both the DFT calculations and crystallographic data of analogous Pd compounds (Table S7, see Supporting Information). The EXAFS fitting revealed an unusually short Pd–N_{apical} distance of 2.501 ± 0.067 Å (Figure 4c) when compared with other square planar Pd(II) complexes. In the analogous molecular complex, a 90° rotation of the apical pyrazolate to both avoid the short Pd–N_{apical} distance and minimize steric interactions between adjacent pyrazolates would be expected, and such a rotation is observed in reported crystal structures of Pd(II) scorpionates.[2,22,28–30] In contrast, the close Pd–N_{apical} distance is preserved in **1** by the rigid Tmp* binding pocket enforced by the MOF.

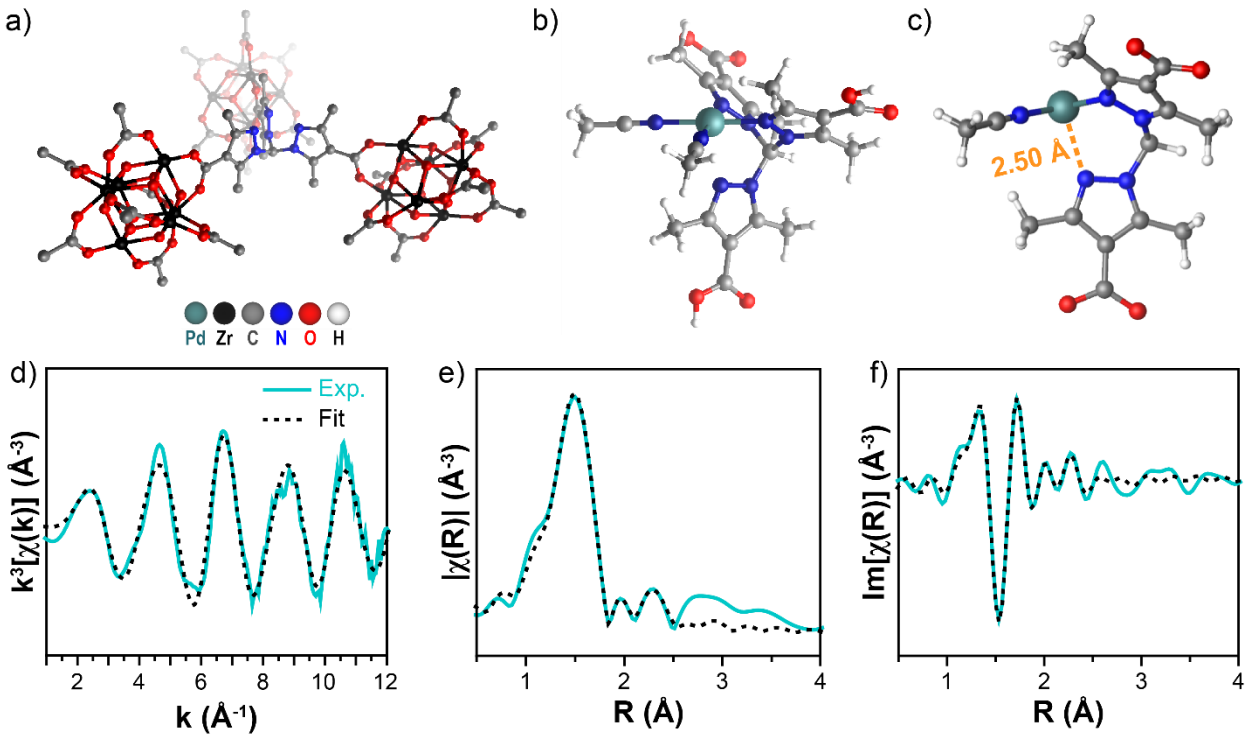

Figure 4. (a) Coordination of TpmC* to Zr-oxo nodes in **1** (protons omitted for visual clarity). (b) Optimized DFT model of $[Pd(CH_3CN)_2TpmC^*]^{2+}$ fragment used for EXAFS fitting. (c) Close Pd-N_{apical} interaction in **2**, determined by EXAFS fitting. (d) k^3-weighted EXAFS signal, and corresponding modulus (e) and imaginary (f) parts of the phase uncorrected FT of the experimental and best fit for $[Pd(CH_3CN)_2TpmC^*]^{2+}$.

Further DFT calculations support the experimentally determined Pd–N_{apical} interatomic separation. Although the original DFT-optimized model predicted a Pd–N_{apical} distance which was approximately 0.2 Å longer than that determined by EXAFS fitting, a subsequent DFT structure optimization in which the Pd–N_{apical} distance was constrained to 2.501 Å raised the structure energy by less than 1 kcal/mol, a marginal increase which falls within the error of DFT calculations. Additionally, we conducted a relaxed potential energy surface (PES) scan, in which geometry optimization occurs at each step prior to energy calculation, across Pd–N_{apical} bond

distances $R_{Pd\text{-}N}$ = (2.301 – 2.801 Å) in 0.04 Å steps at the M06/SDD-6-311G(d,p) level of theory (Figure 5). The calculation revealed a shallow PES between the Pd–N_{apical} distances from EXAFS fitting and DFT optimization, indicating that the experimental data is compatible with calculations.

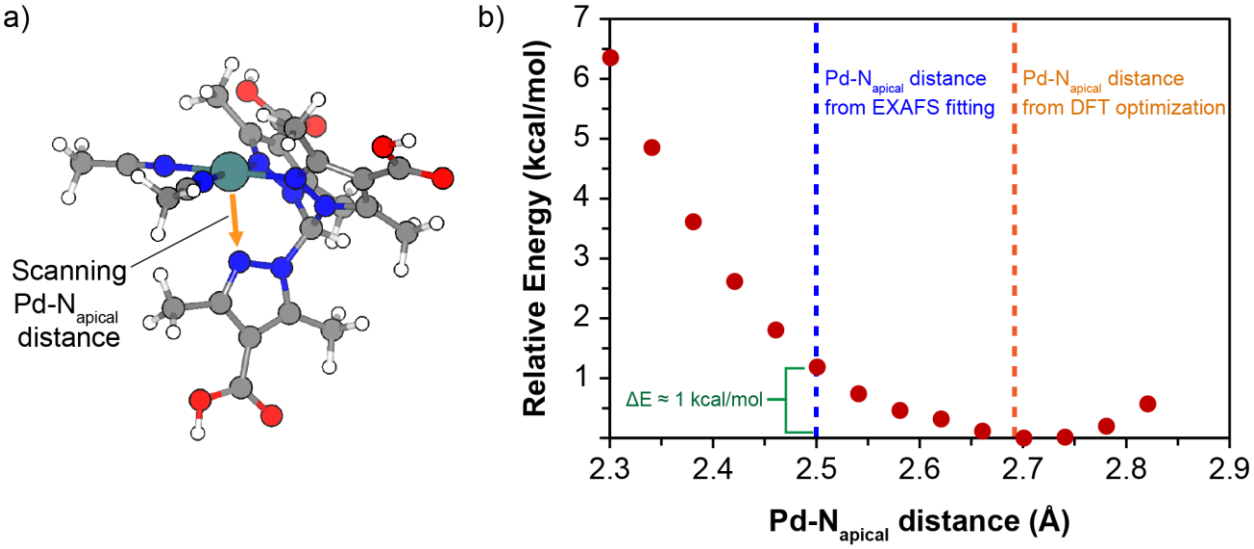

Figure 5. (a) Example structure for $[Pd(CH_3CN)_2(TpmC^*)]^{2+}$ highlighting the Pd–N_{apical} bond. (b) Relative energy (kcal/mol) vs. Pd–N_{apical} distance (Å). A shallow PES surface is observed, which is within the error of DFT calculations.

We thus draw comparison to molecular complexes of Pd(II) with tetradentate diazapyridinophane ligands reported by Mirica et al, where the shortest Pd(II)–N_{apical} distance from X-ray crystal structures (2.525 Å) is slightly longer than the Pd(II)–N_{apical} distance we observed in **1**.[19,20] The close Pd–N_{apical} interaction in the Mirica systems is reported to lower the oxidation potential of Pd and stabilize Pd in the +III and +IV oxidation state, and given the structural similarities, an analogous effect may be present in **1**. High-valent Pd systems find application in catalysis, enabling unprecedented organic transformations not accessible with conventional Pd(0)/Pd(II) systems.[31,32] Yet, to our knowledge, no well-defined Pd(III) or Pd(IV) species have been reported on a solid support, although transient Pd(III) or Pd(IV) has been proposed in the

solid state fluorination catalysis of Pd-functionalized metal-organic layers.[33] Our study of **1** suggests that immobilization of ligands in a MOF in a geometry that preferentially stabilizes Pd(IV) over Pd(II) may be a viable strategy for the development of heterogeneous high-valent Pd catalysts.

Post-Synthetic Installation of Rhodium, Platinum, and Iridium in Zr-TpmC*. Inspired by the successful synthesis of MOF-based Pd scorpionate **1**, we pursued the metallation of Zr-TpmC* by other platinum group metals. We prioritized metallation precursors which have slim steric profiles to allow for facile mass transport into the MOF pores, and/or labile ligands that are easily displaced by the framework-bound scorpionate. Based on these criteria, we chose the metallation precursor $[Rh(CO)_2Cl]_2$ for rhodium, used to generate scorpionate catalysts for C-H bond activation,[3,34,35] and precursors $[Ir(CH_3CN)_2(COD)](BF_4)$ and $[Pt(CH_3CN)_4](BF_4)_2$ for iridium and platinum, respectively. When Zr-TpmC* was soaked in an acetonitrile solution of $[RhCl(CO)_2]_2$ over four days, the MOF sample turned bright yellow to form a product assigned as $[RhCl(CO)_2]$@Zr-TpmC* (**2**). Samples of **2** were prepared with varying amounts of Rh (0.1 – 2.0 equiv / TpmC* site). In contrast to metallation by $[Pd(CH_3CN)_4](BF_4)_2$, the color of the Rh solution did not completely fade, even when sub-stoichiometric quantities of Rh were employed. Correspondingly, metallation of Zr-TpmC* by Rh was not quantitative, with a maximum of 0.4 Rh per TpmC* site installed in **2** (Figure S12). Surface area of Zr-TpmC* also decreases substantially upon metallation by $[Rh(CO)_2Cl]_2$, from 1768 ± 40 m^2/g (Zr-TpmC*) to 701± 1 m^2/g (**2**, 0.4 Rh / TpmC* site). When characterized by PXRD, the intensity of the (200) reflection at 7.8° did not vary with Rh loading, but increasing Rh loading correlated with a pronounced increase in the intensity of the (100) reflection at 3.8° (Figure 6a). Given that the intensity of low angle reflections in the PXRD of MOFs are highly sensistive to disordered species such as solvent in the

pores,[36] the increasing intensity of the (100) reflection for increasing Rh loading in **2** suggests that $[Rh(CO)_2Cl]_2$ is encapsulated in the pores rather than incorporated into the TpmC* site. The small but systematic shift of reflections to lower angles with increasing Rh loading could also be consistent with pore filling, which can subtly distort the MOF structure and increase the size of the unit cell; however, we note that the PXRD in Figure 6a were not referenced to an external standard and the samples were dried at room temperature (and thus not fully desolvated), so there is minor experimental variance in peak position from sample to sample.

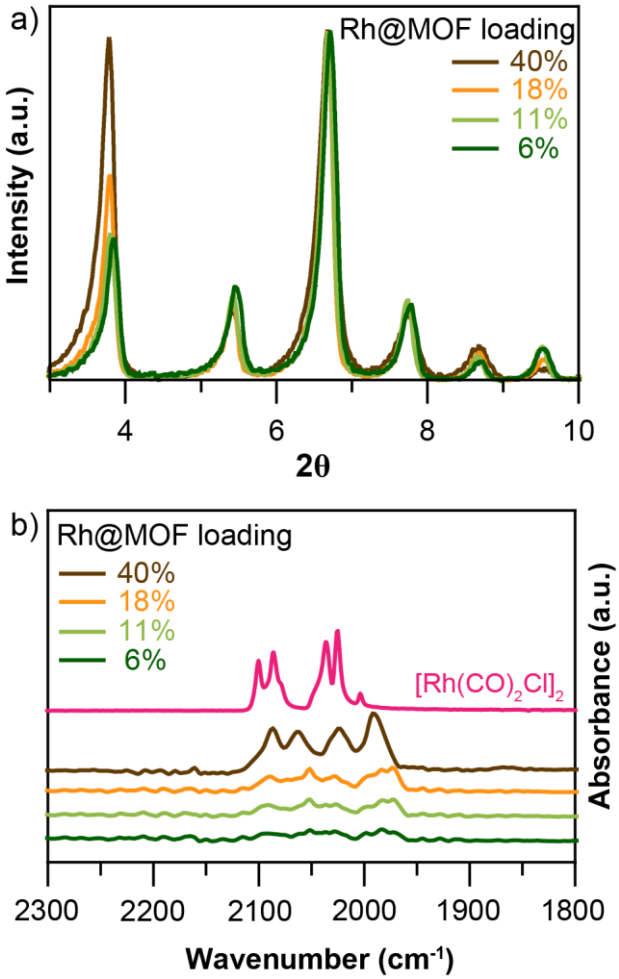

Figure 6. (a) PXRD overlay of Zr-TpmC* samples with varied Rh loading (percentage is vs total accessible TpmC* ligand). (b) FTIR spectrum overlay of Zr-TpmC* samples with varied Rh

loading vs metallation precursor $[Rh(CO)_2Cl]_2$. Rh loading was determined as Rh content vs. available TpmC* sites by ICP-MS.

To better interrogate the Rh speciation in **2**, FTIR were collected for both metallated Rh@MOF samples and the $[Rh(CO)_2Cl]_2$ metallation precursor (Figure 6b). The IR spectrum of $[Rh(CO)_2Cl]_2$ predominantly consists of four strong vibrations related to the carbonyl groups, namely A_1 (2100 cm^{-1}), B_2 (2086 cm^{-1}), B_1 (2037 cm^{-1}), and A_2 (2025 cm^{-1}) vibrations.[37] While the carbonyl vibrations are too weak to resolve for samples of **2** at lower loading, the sample of **2** at 40% loading (equiv. Rh vs. equiv. TpmC* sites) displays four clear vibrations at 2087, 2064, 2023, and 1992 cm^{-1}. We hypothesize that these four vibrations correspond to the four vibrations of the dimeric $[Rh(CO)_2Cl]_2$ metallation precursor, and thus that $[Rh(CO)_2Cl]_2$ maintains its dimeric structure upon incorporation into the MOF. If the TpmC* site were metallated by $[Rh(CO)_2Cl]_2$, the dimer would be expected to break, as is the case for molecular TpmC* complexes. In total, the PXRD, surface area, and FTIR analysis suggest that attempts to generate supported Rh scorpionates in Zr-TpmC* with $[Rh(CO)_2Cl]_2$ instead deposit the Rh dimer intact within the pores.

Metallation of Zr-TpmC* with the third row PGMs iridium and platinum was accomplished under analogous conditions to palladium and rhodium to yield $[Ir(COD)BF_4]$@Zr-TpmC* (**3**, $x \approx$ 0–1.5) and $[Pt(CH_3CN)_2(BF_4)_2]_x$@Zr-TpmC* (**4**, $x \approx$ 0–0.5). As with Pd and Rh, the crystallinity of the MOF is retained and incorporation occurs evenly throughout the material, as determined by PXRD and TEM/EDS, respectively (Figure 1b). However, incorporation of the third-row metals Ir and Pt was substantially lower than the second-row metals, with a maximum of 0.19 Ir per TpmC* site in **3** and a maximum of 0.063 Pt per TpmC* site in **4**. Characterization of **3** and **4** by IR showed no discernible features of the molecular complex, a possible consequence of the low metal loadings.

Direct Synthesis Provides Alternative Route to Access PGM@Zr-TpmC*. Motivated to find synthetic routes which would result in higher metal incorporation for Rh, Ir, and Pt, we hypothesized that TpmC* could be templated *in situ* by metals other than copper for direct MOF synthesis. Anticipating that a d^6 metal would provide the proper geometry for MOF synthesis, we attempted direct synthesis using $IrCl_3$. Indeed, reaction of TpmC* with $IrCl_3$, $ZrOCl_2$, and benzoic acid in DMF at 120 °C over five days yields off-white microcrystalline solids whose PXRD pattern matches Zr-TpmC* and displays no signatures of nanoparticle formation. We assigned these as $IrCl_3$@Zr-TpmC* (**5**) based on ICP-MS data which gives a metal loading of 7.1 equivalents of Ir per formula unit, equivalent to the full metallation achieved post-synthetically with $Pd(CH_3CN)_4(BF_4)_2$.

The rhodium analog, $RhCl_3$@Zr-TpmC* (**6**), can be similarly prepared by direct synthesis of Zr-TpmC* in the presence of $RhCl_3$ (Figure S15). In some preparations, reaction temperatures above 60 °C resulted in blackened material, but no signature of Rh nanoparticles was visible in the powder diffractograms for these samples. The visible blackening of the solids, however, suggests that there may still be nanoparticles present in the sample which are too small to detect by PXRD. Characterization of **6** by TEM/EDS reveals irregular crystallite morphology in contrast to the cubic crystallites of Zr-TpmC* and the PGM-metallated MOF samples (Figure 1b). Rhodium loading in these samples is also sub-quantitative, with 3.5 equivalents of Rh per formula unit installed compared to the theoretical maximum of 8.

Attempts at direct synthesis of Pd@Zr-TpmC* with the Pd(II) precursor Na_2PdCl_4 yielded only Pd nanoparticles, with analogous results for the Pt(II) precursor K_2PtCl_4. We attribute this outcome to two factors. First, the high temperature, acidic conditions, and trace water in the MOF synthesis can decompose DMF to produce amines which readily reduce Pd(II) and Pt(II), leading to rapid

formation and aggregation of Pd^0 and Pt^0 nanoparticles. Second, due to the strong electronic preference of d^8 metals for square planar geometry, coordination of Pd(II) and Pt(II) with TpmC* render the C_{3v} geometry of the ligand higher in energy during synthesis, inhibiting formation of the Zr-TpmC* lattice. Preliminary attempts to access Pt@Zr-TpmC* by direct synthesis using Pt(IV) precursor K_2PtCl_6 yielded grey solids whose PXRD pattern consists of broad peaks which correspond to the Zr-TpmC* structure (Figure S16), but similarly to the Rh direct synthesis, reaction temperature and time were limited by Pt reduction and aggregation. Fortunately, post-synthetic modification avoids the reducing conditions of the MOF synthesis and thus allows for Pd/Pt incorporation into the scorpionate framework without loss of metal to nanoparticle formation.

CONCLUSION

In summary, this work establishes synthetic methodologies for installation of palladium, rhodium, iridium, and platinum into the scorpionate sites of a MOF, while maintaining crystallinity and porosity. We further report the geometrically frustrated interaction between Pd(II) and a scorpionate ligand conformationally locked in C_{3v} symmetry by the MOF superstructure, explored by DFT-assisted EXAFS analysis. An unusually close 2.5 Å Pd(II)–N_{apical} distance was observed which preconfigures the Pd for octahedral geometry and may lower its oxidation potential; further study of Pd@Zr-TpmC* systems may enable access to supported Pd scorpionates in higher oxidation states. Thus, this work not only extends the existing and well-defined chemistry of PGM scorpionates to MOFs, but also signals emergent properties in such systems that can be probed and tuned with high fidelity thanks to the exceptional structural uniformity of MOFs.

EXPERIMENTAL METHODS

Reagents. $ZrOCl_2 \cdot 8H_2O$ and $[Pd(CH_3CN)_4](BF_4)_2$ were purchased from Alfa Aesar. CuI, $AgBF_4$, Na_2PdCl_4, $[Rh(CO)_2Cl]_2$, $RhCl_3$ hydrate, $IrCl_3$ hydrate, $[Ir(1,5\text{-COD})Cl]_2$, $PtCl_2$, K_2PtCl_4, and K_2PtCl_6 were purchased from Sigma-Aldrich. Ethyl diacetoacetate was purchased from TCI. *N*,*N*-dimethylformamide, benzonitrile, acetonitrile, acetone, ethanol and chloroform were used as received without further purification. Ethyl 3,5-dimethylpyrazole-4-carboxylate was synthesized according to a reported procedure.[38] The MOF linker TpmC* was prepared following a previously reported procedure.[18]

Dry, deaerated acetonitrile and dichloromethane were obtained by passing the solvent through two silica columns in a Glass Contour Solvent System and degassing with a flow of Ar gas for 30 min followed by three freeze-pump-thaw cycles. All other commercial reagents were used as received without further purification.

General Procedures. *ICP-MS.* ICP-MS analyses were conducted at the MIT Center for Environmental Health Sciences (MIT CEHS) using an Agilent 7900 inductively coupled plasma mass spectrometer (ICP-MS). Calibration standards were prepared for ICP-MS analysis using analytical standard solutions purchased from Ricca Chemicals and 2% HNO_3 solution (prepared from EMD Millipore Omnitrace® HNO_3 and ultrafiltered water). Digestion of PGM-containing samples was performed in aqua regia (HCl + HNO_3, Omni*Trace* Ultra, EMD Millipore) to ensure digestion of any metallic PGM.

Infrared Spectroscopy (IR). Benchtop IR spectra were recorded on a Bruker Tensor 37 instrument with either a germanium or diamond attenuated total reflectance (ATR) sample holder.

Powder X-ray Diffractometry. Laboratory powder X-ray diffraction patterns were collected on a Bruker D8 diffractometer fitted with a Goebel mirror and a Lynxeye Si strip position-sensitive

detector, operating in reflection mode with Ni-filtered Cu Kα1,2 radiation ($K\alpha_1$ = 1.5406 Å, $K\alpha_2$ = 1.5444 Å, $K\alpha_2$/ $K\alpha_1$ = 0.5). The tube voltage and current were 40 kV and 40 mA, respectively. Samples for PXRD were prepared by placing a thin layer of the appropriate material on a zero-background silicon crystal plate.

Nitrogen Adsorption Measurements. N_2 adsorption isotherms were measured by a volumetric method using a Micromeritics ASAP 2020 Plus gas sorption analyzer. Samples were activated at 110 °C (for demetallated Zr-TpmC* samples) or 95 °C (for metallated Zr-TpmC* samples) under high dynamic vacuum (< 10^{-4} mbar) for 18 hours before analysis. All nitrogen analyses were performed using a liquid nitrogen bath at 77 K. Oil-free vacuum pumps were used to prevent contamination of sample or feed gases. Fits to the Brunauer-Emmett-Teller (BET)[39] equation satisfied the published consistency criteria.[40]

Nuclear Magnetic Resonance. ^{1}H, ^{13}C, and ^{19}F nuclear magnetic resonance (NMR) spectra were measured on a JEOL JNM-ECZ500R/S1 (500 MHz).

X-ray Photoelectron Spectroscopy (XPS). XPS was conducted at Dow Chemical on a PHI VersaProbe II equipped with an Al source using a 100 μm X-ray spot size. Samples were mounted using double sided copper tapes. Charge shift was calibrated by setting either the hydrocarbon C 1s to 285.0 eV, or the Si 2p of SiO_2 to 103.7 eV. Each point of analysis was energy corrected independent of the others.

Scanning Tunneling Electron Microscopy & Energy-Dispersive X-ray Spectroscopy (STEM/EDS). STEM/EDS analysis was conducted at Dow Chemical. Samples for TEM were prepared by mixing a small amount of sample powder with methanol. The fines were collected onto a standard Cu mesh TEM grid with a lacy carbon support. Data collection was performed using a FEI Themis field emission gun (FEG) aberration-corrected (probe) transmission electron

microscope (TEM). The TEM was operated at an accelerating voltage 200 keV. STEM images were collected at 2048 x 2048 image size. The Themis has Bruker AXS XFlash energy dispersive x-ray spectrometer (EDS) detectors with an energy resolution of 137 eV/channel for elemental identification and quantitative analysis. Instrument conditions: STEM 55-100 pA 70 μm C2 Spot 9 for imaging, ~300-500 pA for EDS map collection, 700-1500 second collection time per map, 1024 x 1024 map size.

X-ray Absorption Spectroscopy. X-ray absorption spectroscopy (XAS) measurements in solid state were carried out at the Inner Shell Spectroscopy (ISS) beamline of the National Synchrotron Light Source-II (NSLS-II) at Brookhaven National Laboratory (BNL; Upton, New York). Data was collected at the Pd K-edge (24350 eV) using fluorescence detection with a passivated implanted planar silicon (PIPS) detector. Pellets of 5 mm diameter were pressed from $Pd(CH_3CN)_2(BF_4)_2$@Zr-TpmC* MOF and polyethylene glycol (50:50 ratio by mass).

XAS data reduction and extended X-ray absorption fine structure (EXAFS) extraction procedure were performed using the Athena code, while the EXAFS analysis was done with Artemis software from the Demeter package.[41] Once extracted, the k^3-weighted $\Delta(k)$ functions were Fourier-transformed in the k-space interval $\Delta k = (2.0 – 12.0)$ $Å^{-1}$ and fitted in R-space in the interval $\Delta R =$ (1.0 – 3.1) Å, potentially resulting in 13 independent parameters ($2\Delta k \Delta R/\pi > 13$) (Table S6). Phases and amplitudes were calculated by the FEFF6 code,[42] implemented in the Artemis software, using the density functional theory (DFT) optimized structures.

The first coordination shell of Pd consists of two acetonitrile N atoms and two pyrazole N atoms in square planar geometry, and were modeled as an averaged 4-atom shell of single scattering (SS) paths with a single ΔR and Debye-Waller (σ^2) parameter. due to the close similarity in bond lengths. The SS paths involving N atoms in the second coordination shell were modeled using two

sets of ΔR and σ^2 parameters, one for the two interior N atoms of the coordinated pyrazole rings, and one for the apical N atom of the uncoordinated pyrazole ring.

Synthesis. *Triethyl 1,1',1''-methanetriyltris(3,5-dimethyl-1H-pyrazole-4-carboxylate) (TpmC*-Et).* To a 2 L round-bottom flask containing 50.0 g (297 mmol) ethyl 3,5-dimethylpyrazole-4-carboxylate and 9.60 g (29.8 mmol, 0.1 equiv.) $NBu_4^+Br^-$ was added 320 mL deionized water. 157 g sodium carbonate (1.48 mol, 5 equiv.) was added into the flask in portions. After all sodium carbonate was added, chloroform (360 mL) was added into the flask and the reaction mixture was heated to reflux for 3 days. After the reaction mixture cooled down to room temperature, toluene (400 mL) was added to the flask and the mixture was filtered. The organic phase was collected via separatory funnel, and the aqueous phase was then extracted with toluene (200 mL) three times. The combined organic phases were dried over magnesium sulfate and concentrated to a minimum volume *in vacuo*, after which methanol (ca. 10 mL) was added to induce precipitation of the product. The flask was stored at 4 °C overnight and filtered the following day to recover brown solids. The crude product was washed by sonication in cold MeOH (50 mL), then filtered and dried in air to afford TpmC*-Et as a white powder. Yield: 18.8 g (36.8%). ^{1}H NMR (500 MHz, C_6D_6) δ 8.17 (s, 1H), 4.02 (q, J = 7.1 Hz, 6H), 2.42 (s, 9H), 2.36 (s, 9H), 0.93 (t, J = 7.1 Hz, 9H). ^{13}C NMR (126 MHz, C_6D_6) δ 163.40, 151.16, 145.98, 112.49, 80.86, 59.42, 14.46, 13.88, 10.57.

1,1',1''-methanetriyltris(3,5-dimethyl-1H-pyrazole-4-carboxylic acid) (TpmC)*. In a 1 L round-bottom flask, 19.0 g Na metal was dissolved in 470 mL ethanol stepwise by fully dissolving small pieces of Na (ca. 0.5 g) one at a time. It is important to perform this step slowly and with caution to avoid overheating. Na is highly reactive and poses fire/explosion hazards, and the dissolution of Na in alcohol is exothermic and produces flammable hydrogen gas. After complete dissolution of all Na, 9.18 g TpmC*-Et and 9.40 mL deionized water were added into the solution. The

reaction mixture was then heated to reflux for 30 minutes, during which period the reaction mixture first cleared up then became turbid again. After the reaction mixture cooled down to room temperature, the solid was separated by filtration and redissolved in a minimal amount of deionized water. The mixture was acidified with 7.1 mL of glacial acetic acid and stored at 4 °C overnight. The product TpmC* was isolated by filtration and dried in air overnight to give a white powder. Yield: 6.52 g (84.9 %). ^{1}H NMR (500 MHz, Methanol-d4) δ 8.49 (s, 1H), 2.38 (m, 18H). ^{13}C NMR (126 MHz, Methanol-d4) δ 167.10, 152.98, 147.87, 113.26, 80.85, 14.46, 10.89.

$[CuI(TpmC^*)_8][Zr_6O_4(OH)_4(C_6H_5COO)_4]_3$ (CuI@Zr-TpmC).* In a 1 L glass bottle, 1.49 g TpmC* and 74.0 g benzoic acid (175 equiv.) were sonicated in 500 mL DMF until dissolved to form a colorless solution. Separately, 2.7 g copper (I) iodide (4.0 equiv.) and 2.79 g $ZrOCl_2 \bullet 8\ H_2O$ (2.50 equiv.) were dissolved in 100 mL DMF in a 250 mL glass beaker. The two solutions were then combined in the 1 L glass bottle, which was capped and placed in an oven preheated to 120 °C for 4 days. After cooling down to room temperature, the reaction mixture was filtered through a fine glass frit, collecting fine white solids. The solids were washed on the frit three times with 100 mL DMF and dried on the frit to give a white powder, which was taken directly to the next step. Yield: 3.57 g crude product. The original published procedure[18] heated the reaction mixture to 120 °C for only two days, but we found that extending this reaction time tended to improve crystallinity of the product. This procedure, however, still yielded only microcrystalline product with reaction times as long as 11 days.

$[Zr_6O_4(OH)_4(C_6H_5COO)_4]_3$ (Zr-TpmC).* In a 1 L glass bottle, 3.57 g of as-synthesized Zr-TpmC* was suspended in a mixture of 350 mL DMF and 15 mL 4M HCl. With the bottle capped, the mixture was heated in an oven at 100 °C for 18 hours. After the bottle cooled to room temperature, the solution was decanted. The acid treatment was repeated three more times, and

then the demetallated MOF was isolated by filtration. The solids were washed by soaking in 50 mL DMF for 4 hours, with the solvent decanted and replaced each hour, then the solids were transferred to a 20 mL vial and soaked in DMF overnight. The following day, the solvent was decanted and the solids were soaked in 20 mL acetone for 4 hours, with the solvent decanted and replaced every hour. The MOF was then activated under dynamic vacuum at 110 °C for 18 hours to give a white powder. Yield: 1.204 g (47% versus TpmC*). Cu : Zr = 0.001 : 1.000 as determined by ICP-MS, digested following a reported procedure.

[Ir(1,5-COD)(CH$_3$CN)$_2$]BF$_4$. The Ir(I) metallation complex was prepared following a literature procedure.[43] In a N_2 glovebox, [Ir(1,5-COD)Cl]$_2$ (250 mg, 0.372 mmol) was dissolved into 6 mL of DCM in a 20 mL scintillation vial, forming an orange solution. After 5 min of stirring, 1.5 mL of CH_3CN was added to the solution, which quickly turned yellow. The solution was stirred for 5 minutes to ensure all components were fully dissolved, and then $AgBF_4$ (150. mg, 0.771 mmol) of $AgBF_4$ was added, immediately forming a white-gray precipitate of AgCl. The reaction mixture was stirred for 10 min, then filtered through a glass frit to remove AgCl. An additional ca. 5 mL of DCM was used to rinse the vial and frit. To the yellow filtrate was added ~50 mL of diethyl ether, which caused instantaneous precipitation of fine yellow crystals of [Ir(1,5-COD)$(CH_3CN)_2$](BF_4). The crystals were collected under vacuum on a 15 mL glass frit, washed with two 15 mL aliquots of ether, and left for 5 min to dry. The crystals were transferred to a 20 mL scintillation vial and dried under vacuum overnight (286 mg, 0.609 mmol, 81.8% yield). ^{1}H NMR (400 MHz, $CDCl_3$): δ 1.72 (m, CH2), 2.26 (m, CH2), 2.57 (s, CH3), 4.22 (s, br, CH). ^{13}C NMR (101 MHz, $CDCl_3$): δ 3.50, 31.27, 70.68, 123.19.

Pt(CH$_3$CN)$_2$Cl$_2$. $PtCl_2(CH_3CN)_2$ was prepared from $PtCl_2$ following a slightly modified literature procedure.[44] Under an N_2 atmosphere, $PtCl_2$ (199 mg, 0.748 mmol) was suspended in 25

mL of CH_3CN in a 100 mL Schlenk flask. A magnetic stir bar was added and the reaction mixture was stirred and heated to reflux overnight, during which the $PtCl_2$ fully dissolved to give a pale-yellow solution. The solution was allowed to cool to room temperature and then concentrated *in vacuo* to ca. 10 mL in volume, precipitating yellow solids. Under air, the solids were recovered on a 15 mL glass frit, washed with two 15 mL aliquots of hexanes, and dried overnight under vacuum (203 mg, 0.583 mmol, 78% yield).

$[Pt(CH_3CN)_4](BF_4)_2$. The Pt(II) metallation complex $[Pt(CH_3CN)_4](BF_4)_2$ was prepared with a slight modification of reported procedure[45]. In a N_2 glovebox, a 100 mL Schlenk flask was charged with $AgBF_4$ (230. mg, 1.18 mmol), 20 mL of dry CH_3CN, and a magnetic stir bar. The flask was transferred to a Schlenk line, and $PtCl_2(CH_3CN)_2$ (203 mg, 0.583 mmol) was added under positive pressure of N_2. The hood light was shut off and the flask wrapped in Al foil to mitigate photodegradation of $AgBF_4$, and the reaction mixture was heated to reflux for 4 h under N_2. The reaction mixture was then allowed to cool to room temperature and the foil removed, revealing a yellow solution with a white-grey precipitate of AgCl. Under air, the solution was filtered over a Celite® pad to remove AgCl, and the yellow filtrate was concentrated *in vacuo* to ca. 5 mL. A 50 mL portion of ether was poured into the flask, which caused instantaneous precipitation of fine white crystals of $[Pt(CH_3CN)_4](BF_4)_2$. The product was collected on a 15 mL glass frit, washed with two 10 mL portions of ether, and dried overnight under vacuum. The final product was then transferred to a 20 mL scintillation vial and stored under an N_2 atmosphere (169 mg, 0.317 mmol, 54.4% yield). ^{1}H NMR (400 MHz, CD_3CN): δ 2.61 (s, CH_3). ^{13}C NMR (101 MHz, CD_3CN): δ 4.41.

*General method for post-synthetic metallation of Zr-TpmC**. In an N_2-filled glove box, 100 mg activated Zr-TpmC* is charged into a 20 mL vial. PGM metallation complex (1.0 equiv per TpmC*

site) is dissolved in 10 mL acetonitrile and added into the vial containing Zr-TpmC*. The vial is capped and left undisturbed for 1 week. The metallation solution is decanted and the MOF is soaked in 20 mL fresh acetonitrile overnight to remove unbound metal complex. The supernatant is decanted and replaced with fresh acetonitrile every 24 hours, and the MOF is soaked in fresh acetonitrile for 3 days. The MOF is then soaked in fresh dichloromethane following the same soaking procedure for 3 days. The MOF is then activated at room temperature under dynamic vacuum overnight to give microcrystalline powder.

Metallation of Zr-TpmC by $[Pd(CH_3CN)_4](BF_4)_2$.* Preparation followed the generic procedure, using 100. mg of MOF (0.0171 mmol) and 64.6 mg of $[Pd(CH_3CN)_4](BF_4)$ (0.145 mmol). Elemental analysis: Pd : Zr = 0.378 : 1.000 , as determined by ICP-MS.

Metallation of Zr-TpmC by $[RhCl(CO)_2]_2$.* Preparation followed the generic procedure, using 50. mg of MOF (8.5 μmol) and 13.3 mg of $[RhCl(CO)_2]_2$ (0.0342 mmol). Elemental analysis: Rh : Zr = 0.184 : 1, as determined by ICP-MS.

Metallation of Zr-TpmC by $[Ir(1,5\text{-}COD)(CH_3CN)_2]BF_4$.* Preparation followed the generic procedure, using 100. mg of MOF (0.0171 mmol) and 69 mg of $[Ir(1,5\text{-}COD)(CH_3CN)_2](BF_4)$ (0.15 mmol). Elemental analysis: Ir : Zr = 0.020 : 1.000, as determined by ICP-MS.

Metallation of Zr-TpmC by $[Pt(CH_3CN)_4](BF_4)_2$.* Preparation followed the generic procedure, using 100. mg of Zr-TpmC* (0.0171 mmol) and 78 mg of $[Pt(CH_3CN)_4](BF4)_2$ for the metallation solution. Elemental analysis: Pt : Zr = 0.023 : 1.000, as determined by ICP-MS.

*Direct synthesis of $RhCl_3$@Zr-TpmC**. In a 20 mL scintillation vial, 37 mg rhodium(III) chloride hydrate (0.14 mmol, 1.0 equiv.) and 62 mg TpmC* (0.14 mmol, 1.0 equiv.) were dissolved in 3 mL of DMF/H_2O to form a deep red solution. In a separate 20 mL scintillation vial, 82 mg ZrOCl2•8 H2O (0.25 mmol, 1.8 equiv.) and 2.5 g benzoic acid (20. mmol, 140 equiv.) were

sonicated in 3 mL DMF until dissolved to form a colorless solution. The two solutions were then combined in one vial, which was capped and heated to 60 °C for 24 hours. After cooling down to room temperature, the grey-green solids were collected by centrifugation and washed with three 20 mL portions of DMF, soaking in each wash for at least an hour, followed by two 20 mL portions of acetone, again soaking for at least an hour. Yield: 148 mg unactivated MOF. Elemental analysis: Rh : Zr = 0.166 : 1.000, as determined by ICP-MS.

*Direct synthesis of $IrCl_3$@Zr-TpmC**. In a 100 mL glass bottle, 344. mg iridium(III) chloride hydrate (0.966 mmol, 1.28 equiv.) and 324. mg TpmC* (0.753 mmol, 1.00 equiv.) were dissolved in 10 mL of DMF and stirred for 1 h, forming a deep red/purple solution. In a separate 100 mL Erlenmeyer flask, 555. mg $ZrOCl_2$•$8H_2O$ (1.72 mmol, 2.28 equiv.) and 14.7 g benzoic acid (120 mmol, 159 equiv.) were sonicated in 50 mL DMF until dissolved to form a colorless solution. The contents of the Erlenmeyer flask were then transferred to the glass bottle containing Ir and TpmC*, which was then tightly capped and heated to 120 °C for 4.5 days. After cooling down to room temperature, the yellow supernatant was decanted and the remaining white solids were transferred to a 20 mL scintillation vial. The solids were then washed with three 20 mL portions of DMF, soaking in each wash for at least an hour, followed by two 20 mL portions of acetone, again soaking for at least an hour. The white solids were then activated overnight at 110 °C under high vacuum to yield $IrCl_3$@Zr-TpmC*. Yield: 258 mg activated MOF. Elemental analysis: Ir : Zr = 0.395 : 1.000, as determined by ICP-MS.

*Direct synthesis of K_2PtCl_6@Zr-TpmC**. In a 20 mL scintillation vial, 24.2 mg potassium hexachloroplatinate (0.0498 mmol, 1.00 equiv.) and 22.0 mg TpmC* (0.0511 mmol, 1.03 equiv.) were dissolved in 3 mL of 1:1 DMF/H_2O to form a yellow solution. In a separate 20 mL scintillation vial, 41.3 mg $ZrOCl_2$•8 H_2O (0.128 mmol, 2.50 equiv.) and 1.09 g benzoic acid (8.93

mmol, 175 equiv.) were sonicated in 2 mL DMF until dissolved to form a colorless solution. The two solutions were then combined in one vial, which was capped and heated to 60 °C for 24 hours. After cooling down to room temperature, the grey solids were collected by centrifugation and washed with three 20 mL portions of DMF, soaking in each wash for at least an hour, followed by two 20 mL portions of acetone, again soaking for at least an hour. Yield: 44.1 mg unactivated MOF. Elemental analysis: Pt : Zr = 0.063 : 1.000, as determined by ICP-MS.

Computational Methods. Computational work was performed using the facilities provided by the Massachusetts Green High Performance Computing Center. All calculations were performed with the Gaussian 03[46] program package. Geometry optimization was carried out with the M06 density functional[47], using the 6-311G(d,p) basis set[48] for all nonmetal atoms and the SDD basis set[49] for the Pd atom. The M06 functional was chosen for its enhanced description of dispersion effects. The model structure for optimization by DFT is a truncated cluster model of the formula $[Pd(CH_3CN)_2(TpmC^*)]^{2+}$ (Figure S38). The starting geometry of TpmC* were based on crystallographic data for Zr-TpmC*,[18] and the geometry of Pd^{2+} was assumed to be square planar based on crystallographic data for $[Pd(Tpm)_2](BF_4)_2$ and $[Pd(CH_3CN)_4](BF_4)_2$.[24,28] Structures were allowed to fully optimize such that no imaginary frequencies were observed. Structural rigidity, imparted on TpmC* by the extended structure of the MOF, was modeled by constraining the position of the C and O atoms in the three terminal carboxyls of TpmC* during geometry optimization.

ASSOCIATED CONTENT

Supporting Information. The following files are available free of charge.

NMR data; further PXRD characterization data; XANES results; experimental details and results

on Rh and Pd loading screens; surface area measurements; XPS results; DFT-assisted EXAFS fitting parameters and data; synthetic schemes (PDF)

AUTHOR INFORMATION

Corresponding Author

*Phone: (617) 253-4154. E-mail: mdinca@mit.edu.

ORCID

Mircea DincŠ: 0000-0002-1262-1264

Present Addresses

†CNN: Department of Heterogeneous Catalysis, Max-Planck Institut für Kohlenforschung, Kaiser-Wilhelmplatz 1, 45470 Muelheim, Germany

Author Contributions

The manuscript was written through contributions of all authors. All authors have given approval to the final version of the manuscript.

Funding Sources

This work was supported by funding from the Dow Chemical Company.

Notes

The authors declare no competing financial interest.

ACKNOWLEDGMENT

This research used beamline 8-ID (ISS) of the National Synchrotron Light Source II, a U.S. Department of Energy (DOE) Office of Science User Facility operated for the DOE Office of Science by Brookhaven National Laboratory under Contract No. DE-SC0012704.

We thank James Bour for assistance with DFT calculations, and we thank Amanda Stubbs for assistance with XAS measurements. We also thank Chenyue Sun for providing ligand and MOF samples, and for scientific discussions.

ABBREVIATIONS

DFT, Density Functional Theory; EXAFS, Extended X-ray Absorption Fine Structure; ICP-MS, Inductively Coupled Plasma Mass Spectrometry; IR, Infrared Spectroscopy; MOF, Metal-Organic Framework; NMR, Nuclear Magnetic Resonance; PES, Potential Energy Surface; PGM, Platinum Group Metal (Rh, Ir, Pd, Pt); PXRD, Powder X-ray Diffractometry; SBU, Secondary building unit; SS, Single Scattering; TEM/EDS, Transmission Electron Microscopy / Energy-Dispersive X-ray Spectroscopy; Tp, Trispyrazolylborate; Tpm, Trispyrazolylmethane; XANES, X-ray Absorption Near-Edge Structure; XAS, X-ray Absorption Spectroscopy; XPS, X-ray Photoelectron Spectroscopy.

REFERENCES

(1) Trofimenko, S. Boron-Pyrazole Chemistry. II. Poly(1-Pyrazolyl)-Borates. *J. Am. Chem. Soc.* **1967**, *89* (13), 3170–3177. https://doi.org/10.1021/ja00989a017.

(2) Byers, P. K.; Canty, A. J.; Honeyman, R. T. Organometallic Chemistry of Palladium and Platinum with Poly(Pyrazol-1-Yl)Alkanes and Poly(Pyrazol-1-Yl)Borates. In *Advances in Organometallic Chemistry*; 1992; Vol. 34, pp 1–65. https://doi.org/10.1016/S0065-3055(08)60014-3.

(3) Slugovc, C.; Padilla-martı, I.; Sirol, S.; Carmona, E. Rhodium- and Iridium-Trispyrazolylborate Complexes C H Activation and Coordination Chemistry. *Coord. Chem. Rev.* **2001**, *213*, 129–157. https://doi.org/10.1016/S0010-8545(00)00365-9.

(4) Calabrese, J. C.; Trofimenko, S.; Thompson, J. S. A New Class of Polypyrazolylborate Ligands. *J. Chem. Soc. Chem. Commun.* **1986**, *17* (14), 1122. https://doi.org/10.1039/c39860001122.

(5) Furukawa, H.; Cordova, K. E.; O'Keeffe, M.; Yaghi, O. M. The Chemistry and Applications of Metal-Organic Frameworks. *Science (80-.).* **2013**, *341* (6149). https://doi.org/10.1126/science.1230444.

(6) Brozek, C. K.; DincŠ, M. Thermodynamic Parameters of Cation Exchange in MOF-5 and MFU-4l. *Chem. Commun.* **2015**, *51* (59), 11780–11782. https://doi.org/10.1039/c5cc04249f.

(7) Metzger, E. D.; Brozek, C. K.; Comito, R. J.; Dinca, M. Selective Dimerization of Ethylene to 1-Butene with a Porous Catalyst. *ACS Cent. Sci.* **2016**, *2* (3), 148–153. https://doi.org/10.1021/acscentsci.6b00012.

(8) Comito, R. J.; Metzger, E. D.; Wu, Z.; Zhang, G.; Hendon, C. H.; Miller, J. T.; Dincă, M. Selective Dimerization of Propylene with Ni-MFU-4l. *Organometallics* **2017**, *36* (9), 1681–1683. https://doi.org/10.1021/acs.organomet.7b00178.

(9) Comito, R. J.; Wu, Z.; Zhang, G.; Lawrence, J. A.; Korzyński, M. D.; Kehl, J. A.; Miller, J. T.; Dincă, M. Stabilized Vanadium Catalyst for Olefin Polymerization by Site Isolation in a Metal–Organic Framework. *Angew. Chemie - Int. Ed.* **2018**, *57* (27), 8135–8139.

https://doi.org/10.1002/anie.201803642.

(10) Denysenko, D.; Jelic, J.; Reuter, K.; Volkmer, D. Postsynthetic Metal and Ligand Exchange in MFU-4l: A Screening Approach toward Functional Metal-Organic Frameworks Comprising Single-Site Active Centers. *Chem. - A Eur. J.* **2015**, *21* (22), 8188–8199. https://doi.org/10.1002/chem.201406564.

(11) Denysenko, D.; Grzywa, M.; Jelic, J.; Reuter, K.; Volkmer, D. Scorpionate-Type Coordination in MFU-4l Metal-Organic Frameworks: Small-Molecule Binding and Activation upon the Thermally Activated Formation of Open Metal Sites. *Angew. Chemie - Int. Ed.* **2014**, *53* (23), 5832–5836. https://doi.org/10.1002/anie.201310004.

(12) Stubbs, A. W.; Dincă, M. Selective Oxidation of C–H Bonds through a Manganese(III) Hydroperoxo in Mn II -Exchanged CFA-1 . *Inorg. Chem.* **2019**, *58* (19), 13221–13228. https://doi.org/10.1021/acs.inorgchem.9b02068.

(13) Wang, C.-H.; Gao, W.-Y.; Ma, Q.; Powers, D. C. Templating Metastable Pd 2 Carboxylate Aggregates. *Chem. Sci.* **2019**, *10* (6), 1823–1830. https://doi.org/10.1039/C8SC04940H.

(14) Tu, W.; Xu, Y.; Yin, S.; Xu, R. Rational Design of Catalytic Centers in Crystalline Frameworks. *Adv. Mater.* **2018**, *30* (33), 1–29. https://doi.org/10.1002/adma.201707582.

(15) Drake, T.; Ji, P.; Lin, W. Site Isolation in Metal-Organic Frameworks Enables Novel Transition Metal Catalysis. *Acc. Chem. Res.* **2018**, *51* (9), 2129–2138. https://doi.org/10.1021/acs.accounts.8b00297.

(16) Dhakshinamoorthy, A.; Li, Z.; Garcia, H. Catalysis and Photocatalysis by Metal Organic

Frameworks. *Chem. Soc. Rev.* **2018**, *7*. https://doi.org/10.1039/C8CS00256H.

(17) Drake, T.; Ji, P.; Lin, W. Site Isolation in Metal-Organic Frameworks Enables Novel Transition Metal Catalysis. *Acc. Chem. Res.* **2018**, *51* (9), 2129–2138. https://doi.org/10.1021/acs.accounts.8b00297.

(18) Sun, C.; Skorupskii, G.; Dou, J.-H.; Wright, A. M.; Dincă, M. Reversible Metalation and Catalysis with a Scorpionate-like Metallo-Ligand in a Metal–Organic Framework. *J. Am. Chem. Soc.* **2018**, *140* (50), 17394–17398. https://doi.org/10.1021/jacs.8b11085.

(19) Khusnutdinova, J. R.; Rath, N. P.; Mirica, L. M. The Conformational Flexibility of the Tetradentate Ligand TBu N4 Is Essential for the Stabilization of (TBu N4)Pd III Complexes. *Inorg. Chem.* **2014**, *53* (24), 13112–13129. https://doi.org/10.1021/ic5023054.

(20) Qu, F.; Khusnutdinova, J. R.; Rath, N. P.; Mirica, L. M. Dioxygen Activation by an Organometallic Pd(II) Precursor: Formation of a Pd(IV)-OH Complex and Its C-O Bond Formation Reactivity. *Chem. Commun.* **2014**, *50* (23), 3036–3039. https://doi.org/10.1039/c3cc49387c.

(21) Krieble, V. K.; Noll, C. I. The Hydrolysis of Nitriles with Acids. *J. Am. Chem. Soc.* **1939**, *61* (3), 560–563. https://doi.org/10.1021/ja01872a005.

(22) Canty, A. J.; Hoare, J. L.; Skelton, B. W.; White, A. H.; Van Koten, G. Synthesis and Reactivity of Poly(Pyrazol-1-Yl)Borate Derivatives of Cyclopalladation Systems, Including Structural Studies of Pd{2-CH2C6H4P(o-Tolyl)2-C,P}{(Pz)3BH-N,N′} and Pd(C6H4C5H4N-C2,N′){(Pz)3BH-N,N′}. *J. Organomet. Chem.* **1998**, *552* (1–2), 23–29. https://doi.org/10.1016/S0022-328X(97)00576-7.

(23) Korzyn, M. D.; Braglia, L.; Borfecchia, E.; Lamberti, C.; Dinca, M. Molecular Niobium Precursors in Various Oxidation States: An XAS Case Study. *Inorg. Chem.* **2018**. https://doi.org/10.1021/acs.inorgchem.8b02616.

(24) Edwards, P. G.; Paisey, S. J.; Albers, T. CCDC 101970: Experimental Crystal Structure Determination. *CDC Commun.* **1999**. https://doi.org/10.5517/cc3f3cz.

(25) Maihom, T.; Wannakao, S.; Boekfa, B.; Limtrakul, J. Production of Formic Acid via Hydrogenation of CO2 over a Copper-Alkoxide-Functionalized MOF: A Mechanistic Study. *J. Phys. Chem. C* **2013**, *117* (34), 17650–17658. https://doi.org/10.1021/jp405178p.

(26) Odoh, S. O.; Cramer, C. J.; Truhlar, D. G.; Gagliardi, L. Quantum-Chemical Characterization of the Properties and Reactivities of Metal-Organic Frameworks. *Chem. Rev.* **2015**, *115* (12), 6051–6111. https://doi.org/10.1021/cr500551h.

(27) Ortuño, M. A.; Bernales, V.; Gagliardi, L.; Cramer, C. J. Computational Study of First-Row Transition Metals Supported on MOF NU-1000 for Catalytic Acceptorless Alcohol Dehydrogenation. *J. Phys. Chem. C* **2016**, *120* (43), 24697–24705. https://doi.org/10.1021/acs.jpcc.6b06381.

(28) Canty, A. J.; Minchin, N. J.; Engelhardt, L. M.; Skelton, B. W.; White, A. H. Interaction of Palladium(II) with Polydentate Ligands, Including the Synthesis and Structure of Bis[Tris(Pyrazol-1-Yl)Borato-N,N′]Palladium(II) and the Cations [Pd(L)2]2+ [L = Tris(Pyrazol-1-Yl)Methane-N,N′ or Tris(Pyridin-2-Yl)Methane-N,N′]. *J. Chem. Soc. Dalt. Trans.* **1986**, *0* (3), 645–650. https://doi.org/10.1039/DT9860000645.

(29) Brock, C. P.; Das, M. K.; Minton, R. P.; Niedenzu, K. Pyrazole Derivatives of Diborane(4).

J. Am. Chem. Soc. **1988**, *110* (3), 817–822. https://doi.org/10.1021/ja00211a021.

(30) Mlateček, M.; Dostál, L.; Růžičková, Z.; Honzíček, J.; Holubová, J.; Erben, M. The First Scorpionate Ligand Based on Diazaphosphole. *Dalt. Trans.* **2015**, *44* (46), 20242–20253. https://doi.org/10.1039/c5dt03589a.

(31) Hickman, A. J.; Sanford, M. S. High-Valent Organometallic Copper and Palladium in Catalysis. *Nature*. Nature Publishing Group April 11, 2012, pp 177–185. https://doi.org/10.1038/nature11008.

(32) Sehnal, P.; Taylor, R. J. K.; Fairlamb, I. J. S. Emergence of Palladium(IV) Chemistry in Synthesis and Catalysis. *Chem. Rev.* **2010**, *110* (2), 824–889. https://doi.org/10.1021/cr9003242.

(33) Shi, W.; Zeng, L.; Cao, L.; Huang, Y.; Wang, C.; Lin, W. Metal-Organic Layers as Reusable Solid Fluorination Reagents and Heterogeneous Catalysts for Aromatic Fluorination. *Nano Res.* **2021**, *14* (2), 473–478. https://doi.org/10.1007/s12274-020-2698-8.

(34) Purwoko, A. A.; Lees, A. J. Photochemical C−H Bond Activation Reactivity of (HBPz‘ 3)Rh(CO) 2 (Pz‘ = 3,5-Dimethylpyrazolyl) in Alkane Solutions. *Inorg. Chem.* **1996**, *35* (3), 675–682. https://doi.org/10.1021/ic951199x.

(35) Ghosh, C. K.; Graham, W. A. G. Efficient and Selective Carbon-Hydrogen Activation by a Tris(Pyrazolylborate)Rhodium Complex. *J. Am. Chem. Soc.* **1987**, *109* (15), 4726–4727. https://doi.org/10.1021/ja00249a048.

(36) Øien-ØDegaard, S.; Shearer, G. C.; Wragg, D. S.; Lillerud, K. P. Pitfalls in Metal-Organic

Framework Crystallography: Towards More Accurate Crystal Structures. *Chem. Soc. Rev.* **2017**, *46* (16), 4867–4876. https://doi.org/10.1039/c6cs00533k.

(37) Sizova, O. V.; Varshavskii, Y. S.; Nikol'skii, A. B. Binuclear Rhodium(I) Carbonyl Carboxylate Complexes: DFT Study of Structural and Spectral Properties. *Russ. J. Coord. Chem. Khimiya* **2005**, *31* (12), 875–883. https://doi.org/10.1007/s11173-005-0185-0.

(38) Jung, J. C.; Watkins, E. B.; Avery, M. A. Synthesis of 3-Substituted and 3,4-Disubstituted Pyrazolin-5-Ones. *Tetrahedron* **2002**, *58* (18), 3639–3646. https://doi.org/10.1016/S0040-4020(02)00306-X.

(39) Brunauer, S.; Emmett, P. H.; Teller, E. Adsorption of Gases in Multimolecular Layers. *J. Am. Chem. Soc.* **1938**, *60* (2), 309–319. https://doi.org/10.1021/ja01269a023.

(40) Rouquerol, J.; Llewellyn, P.; Rouquerol, F. Is the BET Equation Applicable to Microporous Adsorbents? *Stud. Surf. Sci. Catal.* **2007**, *160* (December 2015), 49–56. https://doi.org/10.1016/s0167-2991(07)80008-5.

(41) Ravel, B.; Newville, M. ATHENA, ARTEMIS, HEPHAESTUS: Data Analysis for X-Ray Absorption Spectroscopy Using IFEFFIT. *J. Synchrotron Radiat.* **2005**, *12* (4), 537–541. https://doi.org/10.1107/S0909049505012719.

(42) Newville, M. IFEFFIT : Interactive XAFS Analysis and FEFF Fitting. *J. Synchrotron Radiat.* **2001**, *8* (2), 322–324. https://doi.org/10.1107/S0909049500016964.

(43) Whitehead, C. B.; Finke, R. G. Nucleation Kinetics and Molecular Mechanism in Transition-Metal Nanoparticle Formation: The Intriguing, Informative Case of a Bimetallic

Precursor, {[(1,5-COD)Ir I ·HPO 4] 2 } 2-. *Chem. Mater.* **2019**, *31* (8), 2848–2862. https://doi.org/10.1021/acs.chemmater.8b05335.

(44) Fraccarollo, D.; Bertani, R.; Mozzon, M.; Belluco, U.; Michelin, R. A. Synthesis and Spectroscopic Investigation of Cis and Trans Isomers of Bis(Nitrile)Dichloroplatinum(II) Complexes. *Inorganica Chim. Acta* **1992**, *201* (1), 15–22. https://doi.org/10.1016/S0020-1693(00)84996-8.

(45) Muller, T. E.; Green, J. C.; Mingos, D. M. P.; Mcpartlin, C. M. Complexes of Gold ž I / and Platinum ž II / with Polyaromatic Phosphine. **1998**, No. January.

(46) Frisch, M. J.; Trucks, G. W.; Schlegel, H. B.; Scuseria, G. E.; Robb, M. A.; Cheeseman, J. R.; Montgomery, Jr., J. A.; Vreven, T.; Kudin, K. N.; Burant, J. C.; Millam, J. M.; Iyengar, S. S.; Tomasi, J.; Barone, V.; Mennucci, B.; Cossi, M.; Scalmani, G.; Rega, N.; Petersson, G. A.; Nakatsuji, H.; Hada, M.; Ehara, M.; Toyota, K.; Fukuda, R.; Hasegawa, J.; Ishida, M.; Nakajima, T.; Honda, Y.; Kitao, O.; Nakai, H.; Klene, M.; Li, X.; Knox, J. E.; Hratchian, H. P.; Cross, J. B.; Bakken, V.; Adamo, C.; Jaramillo, J.; Gomperts, R.; Stratmann, R. E.; Yazyev, O.; Austin, A. J.; Cammi, R.; Pomelli, C.; Ochterski, J. W.; Ayala, P. Y.; Morokuma, K.; Voth, G. A.; Salvador, P.; Dannenberg, J. J.; Zakrzewski, V. G.; Dapprich, S.; Daniels, A. D.; Strain, M. C.; Farkas, O.; Malick, D. K.; Rabuck, A. D.; Raghavachari, K.; Foresman, J. B.; Ortiz, J. V.; Cui, Q.; Baboul, A. G.; Clifford, S.; Cioslowski, J.; Stefanov, B. B.; Liu, G.; Liashenko, A.; Piskorz, P.; Komaromi, I.; Martin, R. L.; Fox, D. J.; Keith, T.; Al-Laham, M. A.; Peng, C. Y.; Nanayakkara, A.; Challacombe, M.; Gill, P. M. W.; Johnson, B.; Chen, W.; Wong, M. W.; Gonzalez, C.; Pople, J. A. Gaussian 03. Gaussian Inc.: Wallingford, CT 2004.

(47) Zhao, Y.; Truhlar, D. G. The M06 Suite of Density Functionals for Main Group Thermochemistry, Thermochemical Kinetics, Noncovalent Interactions, Excited States, and Transition Elements: Two New Functionals and Systematic Testing of Four M06-Class Functionals and 12 Other Function. *Theor. Chem. Acc.* **2008**, *120* (1–3), 215–241. https://doi.org/10.1007/s00214-007-0310-x.

(48) Krishnan, R.; Binkley, J. S.; Seeger, R.; Pople, J. A. Self-Consistent Molecular Orbital Methods. XX. A Basis Set for Correlated Wave Functions. *J. Chem. Phys.* **1980**, *72* (1), 650–654. https://doi.org/10.1063/1.438955.

(49) Andrae, D.; Häußermann, U.; Dolg, M.; Stoll, H.; Preuß, H. Energy-Adjusted Ab Initio Pseudopotentials for the Second and Third Row Transition Elements. *Theor. Chim. Acta* **1990**, *77* (2), 123–141. https://doi.org/10.1007/BF01114537.